Characterization of Vortex Dynamics in the Near Wake of an Oscillating Flexible Foil

Firas F. Siala
School of Mechanical, Industrial and Manufacturing Engineering,
Oregon State University,
Corvallis, OR 97331

Alexander D. Totpal
School of Mechanical, Industrial and Manufacturing Engineering,
Oregon State University,
Corvallis, OR 97331

James A. Liburdy
School of Mechanical, Industrial and Manufacturing Engineering,
Oregon State University,
Corvallis, OR 97331

An experimental study was conducted to explore the effect of surface flexibility at the leading and trailing edges on the near-wake flow dynamics of a sinusoidal heaving foil. Midspan particle image velocimetry (PIV) measurements were taken in a closed-loop wind tunnel at a Reynolds number of 25,000 and at a range of reduced frequencies ($k = fc/U$) from 0.09 to 0.20. Time-resolved and phase-locked measurements are used to describe the mean flow characteristics and phase-averaged vortex structures and their evolution. Large-eddy scale (LES) decomposition and swirling strength analysis are used to quantify the vortical structures. The results demonstrate that trailing edge flexibility has minimal influence on the mean flow characteristics. The mean velocity deficit for the flexible trailing edge and rigid foils remains constant for all reduced frequencies tested. However, the trailing edge flexibility increases the swirling strength of the small-scale structures, resulting in enhanced cross-stream dispersion. Flexibility at the leading edge is shown to generate a large-scale leading edge vortex (LEV) for $k \geq 0.18$. This results in a reduction in the swirling strength due to vortex interactions when compared to the flexible trailing edge and rigid foils. Furthermore, it is shown that the large-scale LEV is responsible for extracting a significant portion of energy from the mean flow, reducing the mean flow momentum in the wake. The kinetic energy loss in the wake is shown to scale with the energy content of the LEV. [DOI: 10.1115/1.4033959]

Introduction

Growing aero/marine applications for energy harvesting and propulsion have advanced research into animal locomotion [1–5]. The flow physics of swimming and flying animals has received significant attention mostly in the context of developing bio-inspired micro-air vehicles and oscillating flow energy harvesters [6–10]. Many animals, including fish, insects, and birds, exploit complex oscillatory motion for highly efficient maneuvering and aero/hydrodynamic performance. The study of flapping foil devices for propulsion purposes is widely established with applications in micro-air vehicles, autonomous underwater vehicles, and robotic fish [10–15]. However in the past decade, research efforts have extended the key elements of flapping foil locomotion to energy harvesting devices, where the goal is energy extraction rather than energy consumption [16–20]. Studies have shown that oscillating foil energy harvesters are capable of extracting energy from a flow with efficiencies comparable to traditional rotary devices [21,22].

Recently, substantial research efforts have focused on studying mechanisms to further improve the aerodynamic performance of flapping foils in energy consumption as well as energy harvesting regimes. One such mechanism is the use of foils with flexible surfaces, in an attempt to mimic flying and swimming animals. Studies on insect wings and fish fins suggest that flexibility may lead to the generation of higher lift and thrust [23–30]. For example, Heathcote and Gursul [31] demonstrated using PIV and hydrodynamic force measurements that a heaving airfoil with a deformable trailing edge generates stronger trailing edge vortices (TEVs), which results in an enhanced thrust coefficient when compared to a purely rigid airfoil. The direct numerical simulation results by Apte and Base [9], where the trailing edge flexibility is modeled using spring dynamics and allowed to be influenced by the fluid-structure interactions, are in good agreement with the experimental results of Heathcote and Gursul. Apte and Base concluded that in order to maximize the propulsion efficiency, the natural frequency of the trailing edge should be similar in magnitude to the heaving frequency of the airfoil.

In an attempt to further improve energy harvesting efficiencies, the use of flexible surfaces has also received some attention in recent years [9,32–34]. The study by Siala and Liburdy [33] experimentally evaluated the time-resolved aerodynamic load measurements in a combined forward pitching and heaving foil with a passively oscillating trailing edge. Under these conditions, they show that trailing edge flexibility enhances the mean power output by 14%. Liu et al. [34] performed two-dimensional simulations to study the effect of chordwise flexibility of an oscillating hydrofoil. The simulation results showed that leading edge flexibility is beneficial to energy harvesting efficiency by shifting the phase between lift force and heaving velocity to achieve useful power output. On the other hand, trailing edge flexibility is found to enhance the size and strength of the LEV, and thus increases peak lift forces. Bandyopadhyay [35] provides a thorough review of the LEV phenomenon in flapping foil applications in general.

Despite the significant amount of investigations on the influence of surface flexibility on the LEV and lift force generation [35–37], there exist a limited number of detailed experimental studies that describe the effect of flexibility on the wake structure and vortex shedding dynamics. In propulsion applications where high oscillation frequencies are required to generate high efficiencies, the wake structure has been primarily investigated for rigid foil cases [13,14,38–40,41]. Lewin and Haj-Hariri [42] numerically investigated the wake structure of a heaving airfoil at low Reynolds number and at large heaving amplitudes. They found that LEVs shed into the wake when the reduced frequency is within $k = fc/U = 1$ and 4. In this range, discrete vortices are shed and their interaction with the TEVs controls the overall wake structure. They showed that the LEV can either merge with the TEV resulting in two vortices shed per cycle of oscillation, or it can pair up with the TEV, resulting in four vortices shed per cycle. Similar results were shown by Koochesfahani's flow visualization [43]. On the contrary, Lai and Platzer [39] and Young and Lai [44] conducted experimental and computational studies, respectively, to investigate the wake structure of a heaving NACA 0012 airfoil at relatively small heaving amplitude and at a Reynolds number of 20,000. They determined that multiple vortices were

Contributed by the Fluids Engineering Division of ASME for publication in the Journal of Fluids Engineering. Manuscript received November 13, 2015; final manuscript received May 23, 2016; published online July 18, 2016. Assoc. Editor: D. Keith Walters.

shed per half-cycle of oscillation, creating very complicated wake structures which were different from the double-wake structure that was found in Ref. [42]. The simulation of Young and Lai [44] showed that the boundary layer on the top and bottom surfaces of the airfoil only separated at the trailing edge, resulting in a blunt-edged body at the trailing edge. The degree of bluntness varies throughout the oscillation cycle, depending primarily on the oscillation frequency and heaving amplitude. Due to the low effective angle of attack generated by the low heaving amplitude ($h = A/c = 0.025$), the airfoil acts as a blunt body and thus has a natural vortex shedding frequency. Young and Lai suggested that the complicated wake structure was a result of the interaction of the natural vortex shedding with the periodic vortex shedding associated with airfoil oscillation.

Motivated by the aforementioned investigations, an examination into the effect of surface flexibility on the near-wake flow dynamics of a purely heaving foil at a low heaving amplitude has been performed. The objective of this work is to characterize the effect of foil flexibility at the leading and trailing edges of a foil on the near-wake flow structures. In addition, a relationship between the LEV (the main source of energy) and the mean kinetic energy loss in the wake is developed. To the best of the authors' knowledge, no such relationship has been identified to date. Velocity measurements were obtained based on time-resolved and phase-resolved PIV in the near-wake region. The time-resolved data are used to identify the overall wake structure, whereas the phase-resolved results are used to determine the evolution of flow structure in the heaving cycle. Furthermore, swirling strength analysis and LES decomposition are used to quantify the vortex statistics (strength, size, etc.). These data are then further used to quantify the energy deficit content in the wake as compared with the energy content of the LEV to determine its contribution to total energy extraction.

The paper first describes the experimental approach; then the results of the mean velocity and vorticity distribution are presented; this is followed by phase-averaged vorticity distribution at various locations during the oscillation cycle; and then the LES, swirl analysis, and velocity autocorrelations are used to quantify vortex statistics in the near wake. Finally, the paper concludes with a vortex scaling analysis showing how the large-scale structures contribute to energy extraction from the mean flow.

Methodology

The experiments were conducted in a closed-loop wind tunnel located at Oregon State University using PIV, as shown in Fig. 1(*a*). The wind tunnel test section cross-sectional area is 1.37 m × 1.52 m with turbulence intensities less than 1%. A flat-plate foil constructed from PC-ABS with a chord of 200 mm, span of 400 mm, and thickness of 6.5 mm (3.3% of chord) was used. The foil, as shown in Fig. 1(*b*), is comprised of two separate edges which attach to the main body using a torsional hinge. The leading and trailing edges each have an elliptical edge with a 5:1 major to minor axis ratio and are each one-third of the total chord length. A

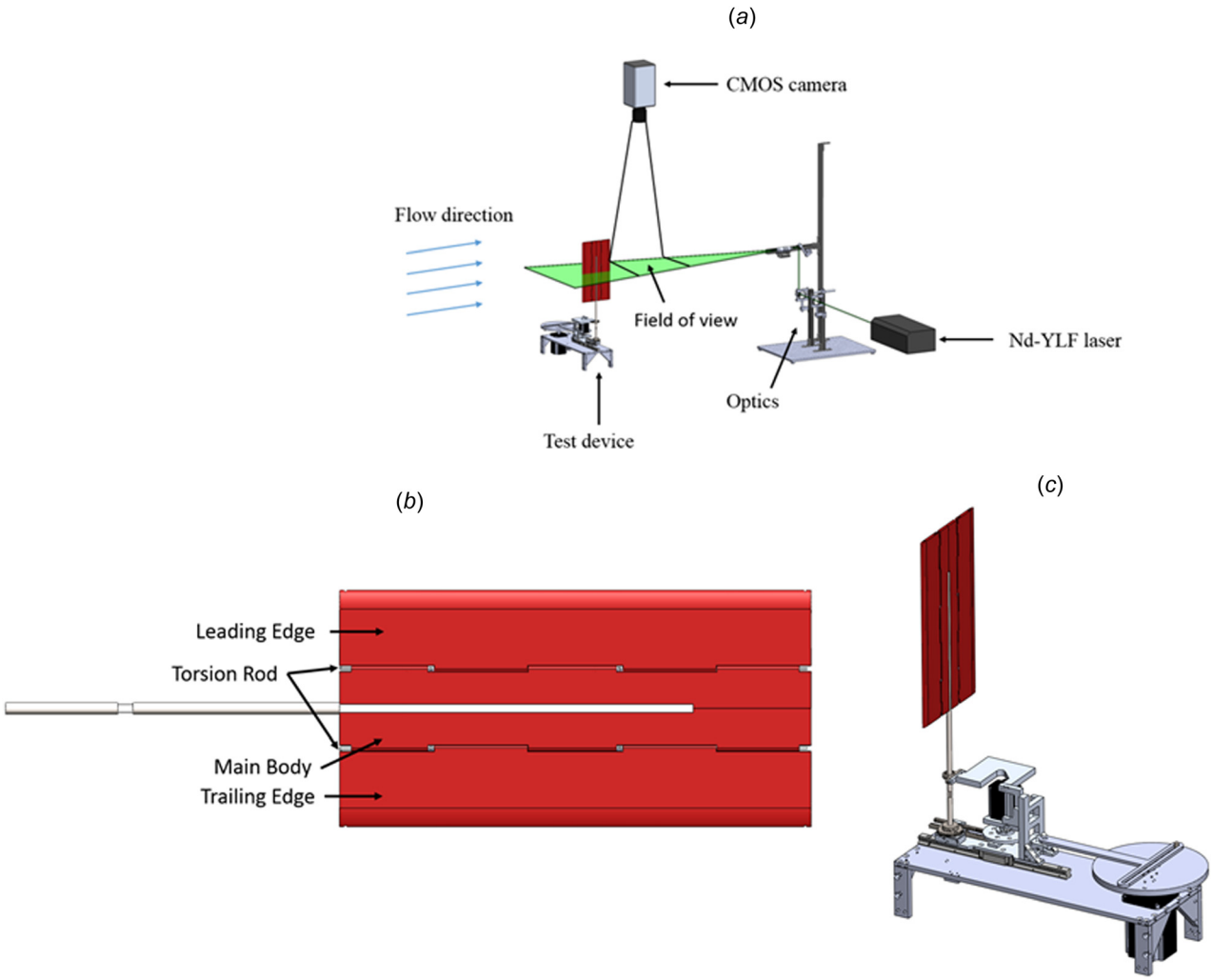

Fig. 1 Cartoons of (*a*) the PIV setup in the wind tunnel, (*b*) side view of the foil indicating the flexible leading and trailing edges, and (*c*) motion control device

1.4 mm diameter steel rod serves as the hinge joint as well as a torsional spring allowing passive surface flexibility on the foil edges as it undergoes the heaving motion. The motion device, as shown in Fig. 1(*c*), uses a stepper motor (resolution of 1.8 deg) and scotch-yoke mechanism to generate the sinusoidal heaving motion. All device controls are performed using LABVIEW. In addition, the foil is attached to the motion device using a titanium rod and is a minimum of 15 cm away from any obstruction from the apparatus.

Two-component, time-resolved and phase-resolved, PIV measurements at the midspan of the foil were obtained for a range of reduced frequencies ($k = fc/U = 0.09$–0.20, where c and U are chord length and freestream velocity, respectively) and at a fixed Reynolds number ($\mathrm{Re}_c = Uc/\nu = 25{,}000$). The heaving amplitude was fixed at $A/c = 0.125$. For each oscillation frequency, the foil was tested under three configurations: fully rigid, flexible leading edge (LE), and flexible trailing edge (TE).

A dual-head Nd-YLF (New Wave Research Pegasus PIV) pulsed laser operating at the 527 nm wavelength is used to generate the light sheet. A series of optical lenses (Dantec Dynamics 9080×0651) and mirrors were used to condition the beam to obtain a 1.5 mm thick light sheet generated in the near wake of the foil. Plexiglas windows on the top of the wind tunnel were used for camera optical viewing. Images were collected using an Integrated Design Tools, Inc. (Pasadena, CA) MotionProTM X-3 CMOS 1280×1024 resolution camera with a built-in intensifier. The camera was equipped with a Nikon AF Micro-NIKKOR, 60 mm adjustable focusing lens with an *f*-number of 2.8 and a magnification of 0.078, resulting in a field of view of approximately 196×157 mm in the near wake of the foil. Seeding particles were generated by atomizing canola oil using a Laskin nozzle, resulting in particle sizes of approximately 2.5 pixels with a final seeding density of approximately 12 seeds per window.

DYNAMICSTUDIO software was used to synchronize the camera and laser pulses. The time between laser pulses varied from 400 to 540 μs depending on the heaving frequency, resulting in about 5 pixel displacement for the highest two reduced frequencies tested (in order to reduce out of plane motion) and 8 pixel displacement for all other frequencies. Particle displacements were determined using a multigrid, multipass adaptive cross-correlation with a central differencing window offset. Adaptive correlation window sizes varied from 128×128 pixels to 32×32 pixel window using a 50% overlap. This resulted in a 79×63 vector field grid points and a vector spacing of 2.4 mm (1.2% of chord). A high-accuracy subpixel peak fitting algorithm specific to Dantec was used. In order to eliminate reflections due to laser scattering from the foil, 14 vector columns were masked near the trailing edge. Minimum peak validation of 1.2 (ratio between the highest to second highest correlation peaks) was performed, and a velocity range validation of ± 4 m/s was implemented to eliminate spurious vectors, resulting in a maximum of 5% rejected velocity vectors. These vectors were replaced using a 3×3 moving average. Time-averaged velocities were collected from 1000 image pairs sampled at 22.5–50 Hz depending on heaving frequency, resulting in 40 complete oscillations for each run. The errors due to particle size, particle displacement, and in-plane loss of pairs were combined using root sum square to calculate the total uncertainty (Table 1). Following the techniques of Westerweel [45], the errors due to velocity gradients and out-of-plane motion were negligible. The total uncertainty in displacement is ~1.32% in the longitudinal direction and ~2.78% in the transverse direction.

For phase measurements, a signal generated by LABVIEW triggered the PIV system at the required heaving phase. The data were collected using 400 image pairs at four phases: $\Phi = 0$ deg, 90 deg, 180 deg, and 270 deg, which correspond to top, mid-downstroke, bottom, and midupstroke heaving positions, respectively. It was found that the foil position varied by ± 6 pixels across all images. In addition, the evolution of a LEV was further studied at the highest reduced frequency case for the flexible LE foil and is evaluated at phase angles of $\Phi = 0$–315 deg in 45 deg increments.

Table 1 Uncertainty estimates

Error source	Δx	Δy
Maximum displacement (pixels)	5.44	2.57
RMS error due to particle size (pixels)	0.070	0.070
RMS error due to particle displacement (pixels)	0.012	0.010
Bias error due to in-plane loss of pairs (pixels)	0.010	0.010
Total error (pixels)	0.072	0.071
Total error (% of max.)	1.32	2.78

RMS: root-mean-square.

Results

Motion Dynamics. The oscillatory motion of the foil used in this study consists of sinusoidal heaving, prescribed according to the following equation:

$$y(t) = \frac{A}{2}\sin(2\pi ft) \tag{1}$$

where A is the total heaving amplitude, f is the oscillation heaving frequency, and t is time. To verify the instantaneous heaving position, fiducial marks were placed on the side edges of the foil, and a digital camera with 1280×1080 pixel resolution at a frame rate of 120 Hz was used in conjunction with image processing software to track the foil position. Similarly, the LE and TE deflection angles were recorded during the oscillation cycle. The results for three oscillation cycles are shown in Fig. 2. Positive deflection angles indicate that the flexible LE and TE are deflected upward relative to the foil body. Additionally, both the flexible LE and TE show a similar deflection transient, indicating that the LE and TE motion is primarily inertia driven with negligible contributions due to fluid–structure interactions. When the foil changes direction in the heaving cycle, the inertia of the LE and TE generates a peak in the deflection angle in the opposite direction of the motion. The torsional spring in this study results in a maximum deflection angle of approximately 5 deg, 18 deg, and 30 deg for $k = 0.12$, 0.18, and 0.2, respectively.

Mean Flow Characteristics. The time-resolved PIV data were used to determine the mean velocity deficit within the near-wake region of the foil. Figure 3 shows the time-averaged velocity distribution at $x/c = 0.2$ and 0.5 behind the foil for $k = 0.12$, 0.18, and 0.2. At $x/c = 0.2$ and $k = 0.12$, the velocity distributions for the flexible LE and rigid cases closely resemble each other, with two distinct peaks located near the maximum and minimum heaving position. The foil with a flexible TE also displays two distinct

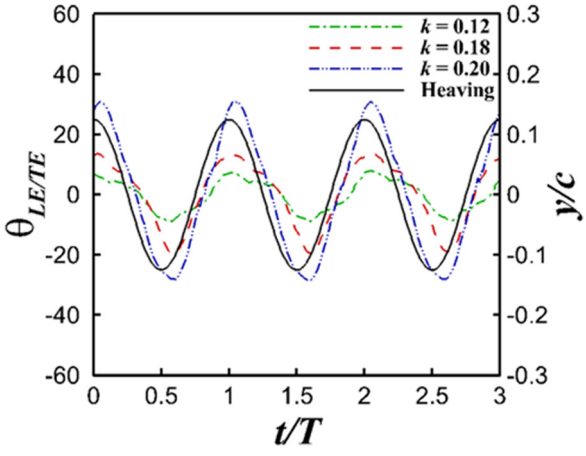

Fig. 2 Measured instantaneous heaving position as well as the leading and trailing edge deflection angles for $k = 0.12$, 0.18, and 0.2

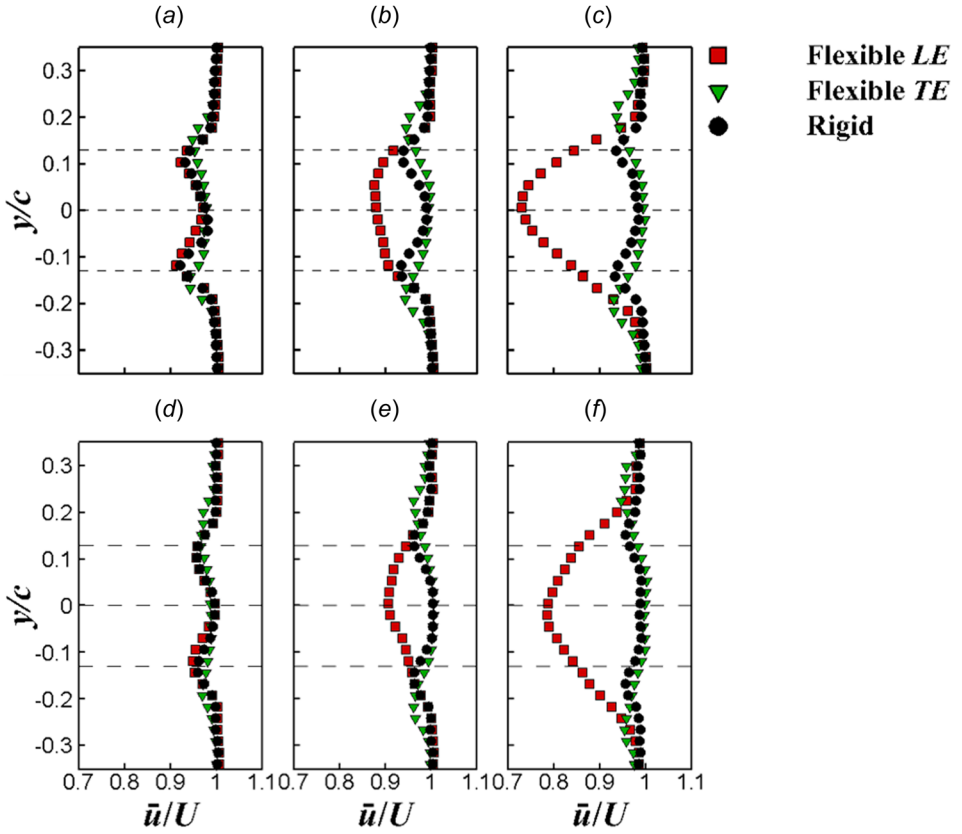

Fig. 3 Mean velocity profiles in the near wake: top row—velocity profile at $x/c = 0.2$ for (*a*) $k = 0.12$, (*b*) $k = 0.18$, and (*c*) $k = 0.2$; bottom row—velocity profile at $x/c = 0.5$ for (*d*) $k = 0.12$, (*e*) $k = 0.18$, and (*f*) $k = 0.2$

peaks; however, the peak locations are slightly above and below the maximum and minimum heaving positions, respectively. This indicates that the flexible TE case results in a greater lateral dispersion than the rigid foil. As the reduced frequency increases, the separation distance between the two peaks generated by the flexible TE foil continues to grow, whereas it remains constant for the rigid foil. Conversely, as k increases, the velocity profile associated with the flexible LE foil shifts from two distinct peaks to a single large peak at the centerline. The size of these peaks increases with increasing reduced frequency, thus indicating a greater mean momentum loss. Although not shown, similar velocity distribution trends are seen at $x/c = 0.5$ as the flow progresses downstream. It can be concluded that the mean velocity deficit is significantly altered by the flexible LE, resulting in large velocity deficit across the entire wake. In contrast, the flexible TE provides some lateral dispersion without changing the magnitude of velocity deficit relative to the rigid foil for the tested range of reduced frequencies.

These observations can be explained by examining the vorticity distribution. Figure 4 shows a contour plot of the mean vorticity distribution (normalized by chord length, c, and freestream velocity, U) for the three foil configurations. For $k = 0.12$, the flexible LE foil generates four distinct vortex sheet layers. Each two adjacent layers form a von Kármán vortex street, centered near the maximum and minimum heaving positions. In each vortex street, the vorticity of the top row is negative (clockwise) and the vorticity of the bottom row is positive (counterclockwise). According to Biot–Savart law, this vortex interaction results in an induced velocity in the opposite direction of the freestream flow. This is indeed observed in Fig. 3(*a*) at the top and bottom heave positions.

As the reduced frequency increases to $k = 0.18$, the flexible LE foil is seen to switch to a single pair of vortex sheet layers with clockwise and counterclockwise rotating vortices aligned with the top and bottom heaving positions, respectively. The effect of this formation is clearly shown in Fig. 3(*b*), where the velocity profile for the flexible LE foil has a single peak deficit, centered at the midheaving position. When the reduced frequency increases further to $k = 0.2$, an increase in size of the same vorticity pattern is observed, resulting in an even greater velocity reduction in the mean flow, as shown in Fig. 3(*c*). The shift of the wake vorticity distribution from a dual to a large single vortex street pattern is clearly responsible for the larger mean flow energy deficit, as is further discussed later.

In contrast, for the flexible TE foil, two von Kármán vortex streets are observed in all the tested reduced frequencies. Also, it can be seen from the vorticity distribution that as the reduced frequency increases, the two vortex streets are angled laterally outward, consistent with the observed lateral dispersion in the velocity profile in Fig. 3. The rigid foil shows a similar behavior to that of the flexible TE, however without the increased lateral dispersion with increasing k. Furthermore, for all foil configurations and reduced frequencies, the vorticity strength decays with increasing distance away from the trailing edge, which is consistent with the smaller velocity deficit at $x/c = 0.5$ when compared to $x/c = 0.2$ shown in Fig. 3.

Phase-Averaged Flow Characteristics. In order to better understand the "reverse bifurcation" or "vortex street coalescence" that occurs with increasing reduced frequency for the flexible LE case, it is useful to investigate the vorticity evolution at different phases in the oscillation cycle for the larger values of k. Figure 5 shows the phase-averaged vorticity distribution at four different phases through the cycle for $k = 0.2$. When the flexible LE foil is at the top heaving position ($\Phi = 0$ deg), a large

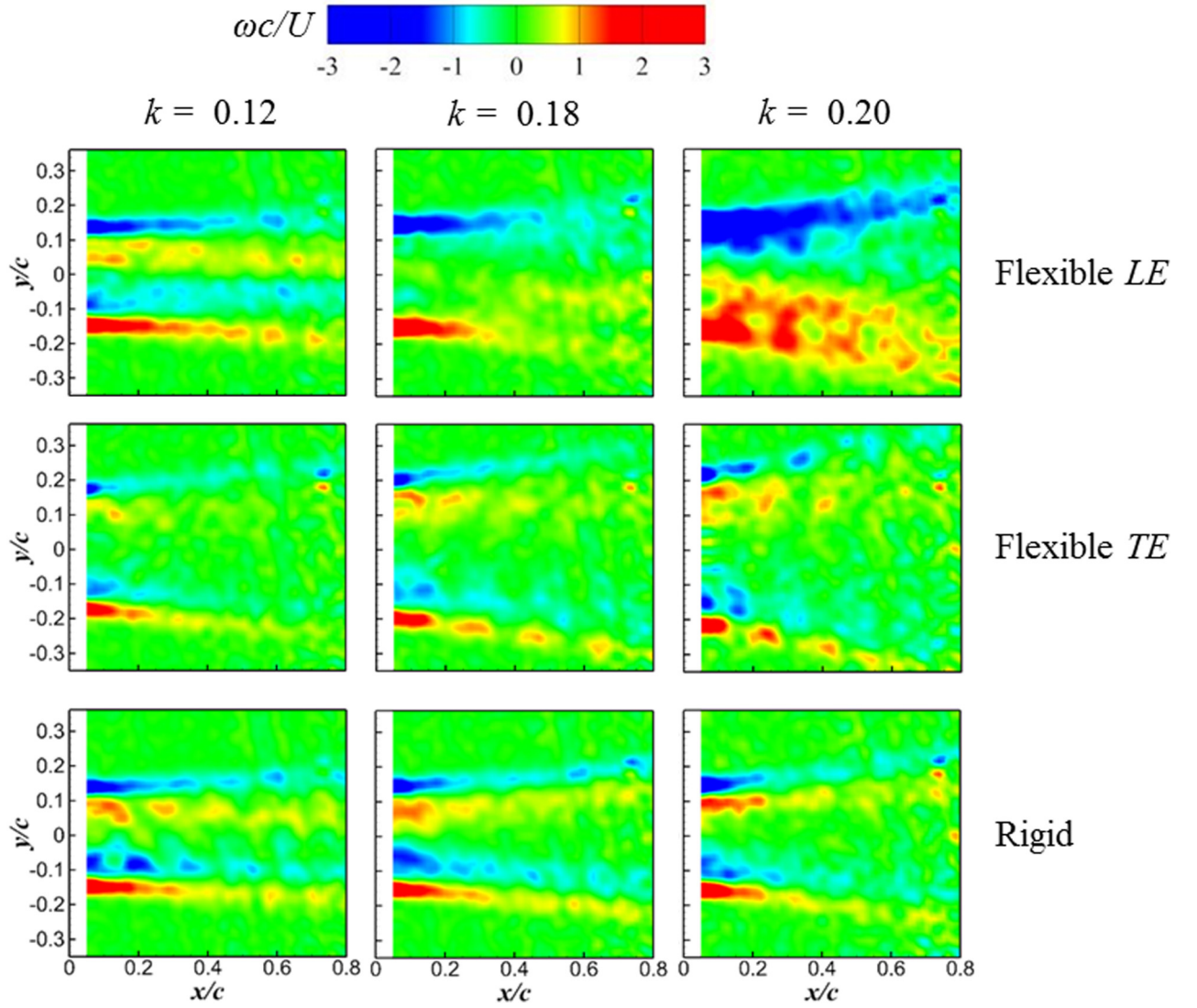

Fig. 4 Mean vorticity contour for the flexible LE, TE, and rigid foil cases at $k = 0.12$, 0.18, and 0.2

counterclockwise LEV is shed from the bottom surface of the leading edge into the wake due to the additional deflection motion of the leading edge, θ_{LE}, as shown in Fig. 2. This angle is significantly greater for large values of k, which causes leading edge separation and the formation of the LEV. During the mid-downstroke ($\Phi = 90$ deg), the vorticity sheds at the trailing edge in a fashion similar to a blunt body. However, the downward momentum of the foil results in the bottom vortex sheet layer to deflect downward, away from the top layer. Similarly, when the foil reaches the bottom heaving position ($\Phi = 180$ deg), another LEV rotating in the clockwise direction is shed from the leading edge. At the midupstroke position ($\Phi = 270$ deg), the vortex pattern is similar to the downward stroke at $\Phi = 90$ deg except with opposite rotation.

The LEV evolution for the flexible LE foil at $k = 0.2$ is shown in more detail in Fig. 6. It is seen that two counter-rotating LEVs form per oscillation cycle, marked as LEV 1 and LEV 2, at the top and bottom heaving positions ($\Phi = 0$ deg or 180 deg, respectively). The center of the detected LEV at these two heaving positions is located at $x/c \approx 0.1$. With the knowledge of the convective velocity of LEV, the time at which it sheds can be approximated. Assuming that the LEV convects at a constant velocity equal to $u_{conv}/U \approx 0.83$, as is shown later, and with the assumption that the center of the LEV is located near the leading edge of the foil, the LEV sheds about 0.135 s before the $\Phi = 0$ deg and 180 deg heaving positions, which corresponds to $\Phi = 270$ deg and 90 deg, respectively. This is expected because the LE deflection angle at $\Phi = 270$ deg and 90 deg is very small (nearly zero), and thus, the adverse pressure gradient along the foil is small, allowing the LEV to convect downstream. Furthermore, using the same estimated convection velocity as stated above, the LEV position at $\Phi = 45$ deg and 225 deg was calculated to be at the "+" position shown for these two phases in Fig. 6. The predicted locations fall very closely to the center of the region of high vorticity for these two phases, supporting the assumption of LEV convection. In addition, the interaction between the LEV and vorticity shed from the trailing edge may be related to the lateral dispersion of these vortex sheets in the subsequent phases at $\Phi = 90$ deg and 270 deg. This is further evidenced by the observation that these vortex sheets return to be more aligned along the flow direction as shown at $\Phi = 135$ deg and 315 deg.

For the flexible TE and rigid foil cases, LEV shedding into the wake is not observed and a very different flow structure exists (see Fig. 5). At the top heaving position, the flexible TE foil increases the strength of the clockwise rotating vortices along the top of the vortex street. This is because the TE is deflected upward (Fig. 2), resulting in a large positive vertical velocity gradient just above the tip of the trailing edge. Whereas for the rigid case, both vortex rows have a similar strength of vorticity. A similar observation is seen at the bottom heaving position, where the flexible

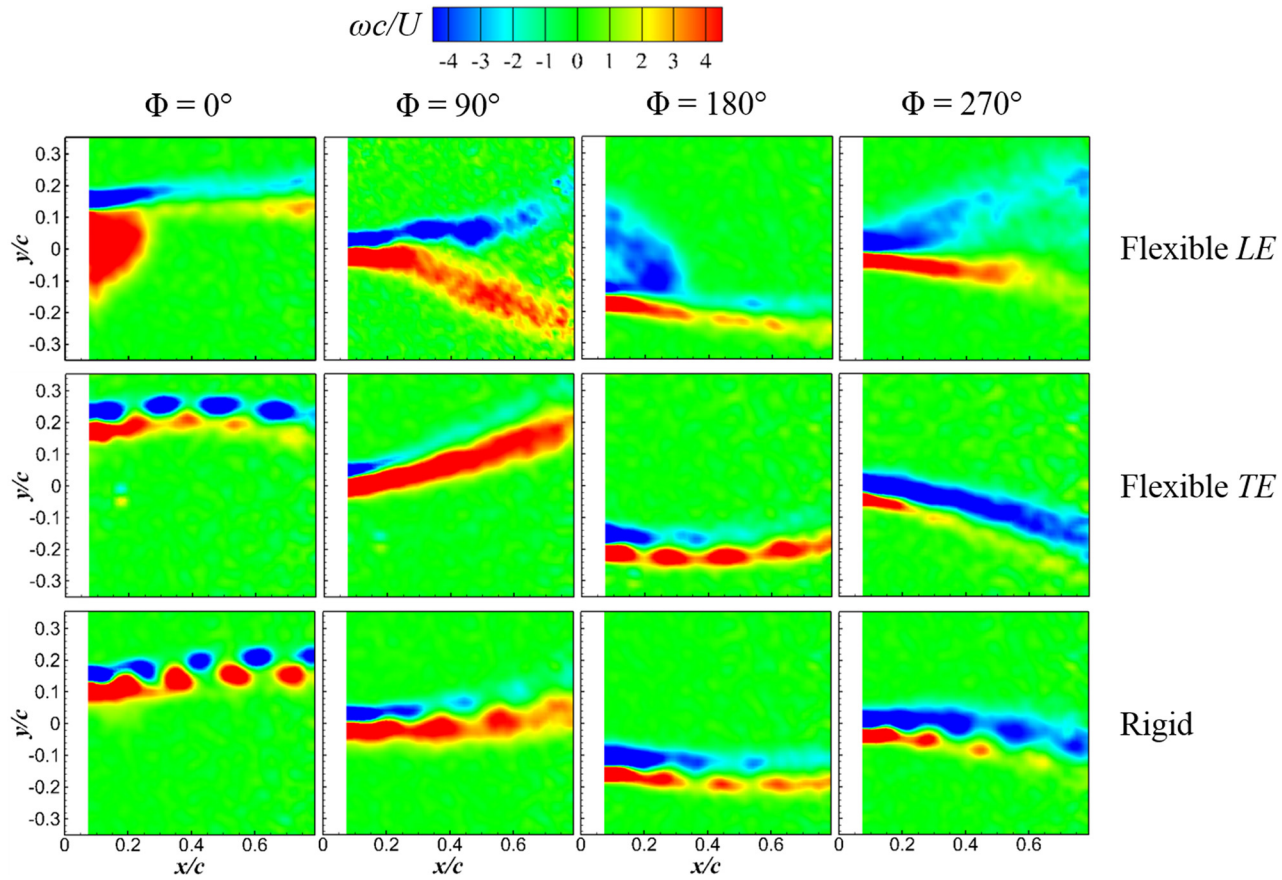

Fig. 5 Phase-averaged vorticity distribution at $k = 0.2$ for flexible LE, TE, and rigid foil cases

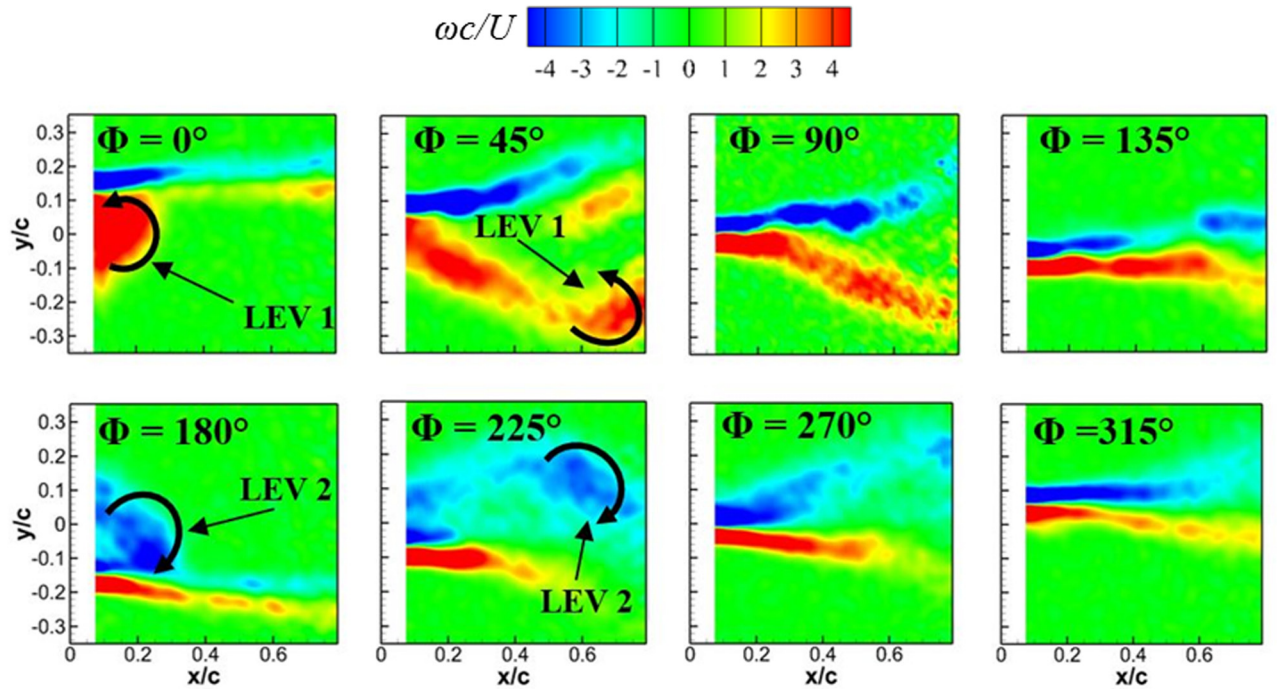

Fig. 6 Phase variation of vorticity distribution in the near wake for $k = 0.2$ for the flexible LE foil; the cross shown for $\Phi = 45$ deg and $\Phi = 225$ deg indicates the predicted location of LEV 1 and LEV 2 which matches the observed region of high vorticity at these phases

TE foil increases the strength of the counterclockwise rotating vortices. In both cases, at the mid-downstroke, the vorticity of the bottom row is stronger than that of the upper row, which is a consequence of the large negative velocity gradient near the trailing edge tip due to the large downward heaving velocity. The opposite is observed during the midupstroke, where the vorticity in the top row is greater than that of the bottom due to the large positive velocity gradient. This results in greater entrainment and larger lateral dispersion for the flexible TE case, as compared with the rigid foil.

Wake Vortex Scaling Characteristics. The large amount of shear present in the flow, especially due to the deflection of the LE and TE at high reduced frequencies, requires vortex detection methods that are insensitive to shear in order to identify and quantify vortical flow structures more accurately. Here, the swirling strength, λ_{ci}, based on critical point analysis, as defined by Zhou et al. [46], is used. The swirling strength is based on the complex conjugate of the eigenvalues of the local velocity gradient and is a measure of the inverse of the time required to complete one revolution of a vortex element. In addition, LES decomposition [47] is also applied which acts as a low-pass filter to the velocity field, which can then be subtracted from the instantaneous velocity field to identify small-scale vortex structures. Consequently, the low-pass filtered field contains the large-scale structures. In this study, the low-pass filtering is performed using a top hat moving average with a filter size 15×15 ($0.18c \times 0.18c$) grid points. Instantaneous small-scale flow structures at the top heaving position and $k = 0.2$ are shown in Fig. 7 for the three foil configurations. The results show that the flexible LE foil, as shown in Fig. 7(*a*), sheds multiple discrete vortices from the leading edge, rather than a single large coherent structure, as is indicated by the phase-averaged vorticity distribution in Fig. 5. The phase averaging used to identify the LEV of Fig. 5 eliminates the smaller scale swirling events inside the LEV, which appear to be random in nature. The instantaneous small-scale LES filtered results for the case of the flexible TE, when the foil is at the top of the heaving position, are shown in Fig. 7(*b*). In good agreement with the phased-averaged vorticity results, the top vortex row has larger swirling strength values compared with the bottom vortex row. Additionally, the rigid foil results in Fig. 8(*c*) show that the swirling strength is roughly equal in both vortex rows, which is again in good agreement with the phased-averaged vorticity results.

The LES low-pass filtered velocity fields are used to identify instantaneous large-scale events. The results for $k \geq 0.18$, overlaid with swirling strength calculations made with the filtered velocity field, are given in Fig. 8 for the flexible LE case. Note that the

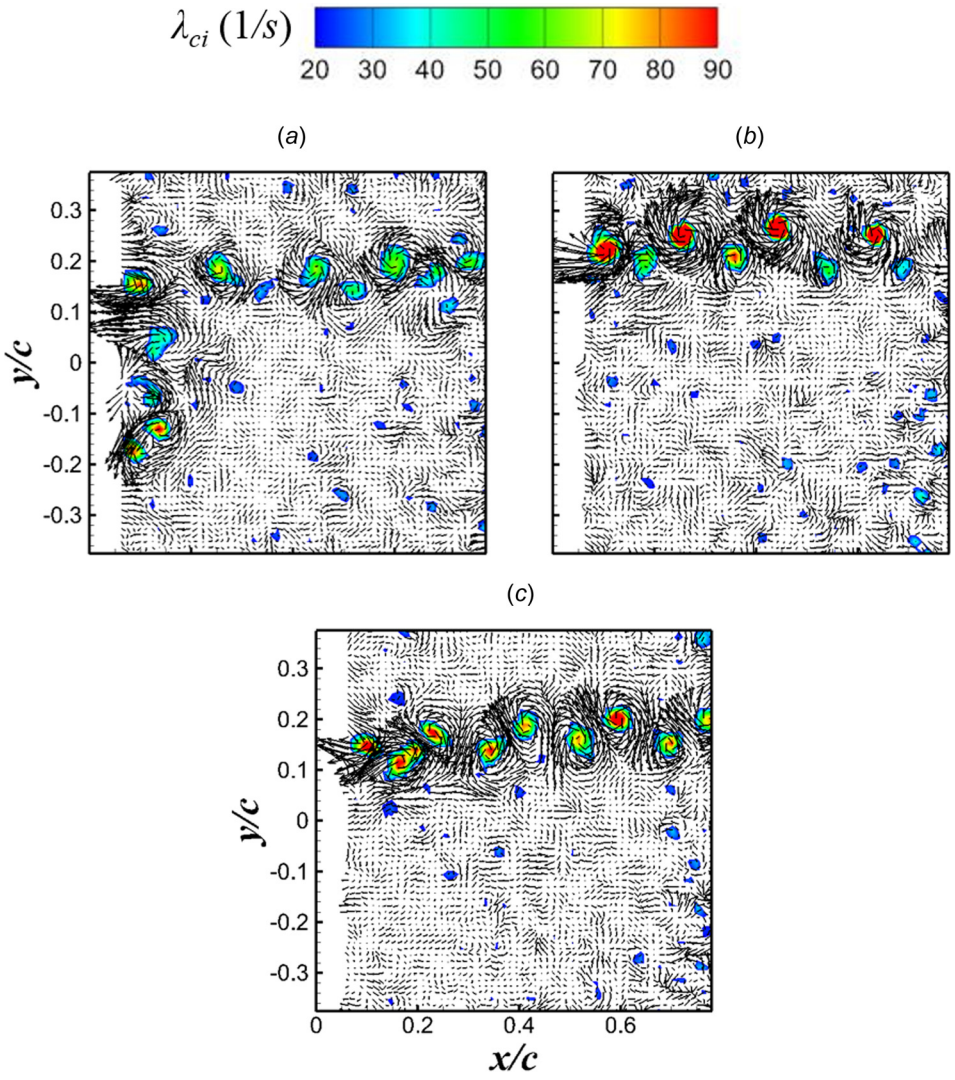

Fig. 7 Instantaneous small-scale LES filtered flow field at the top heaving position ($\Phi = 0$ deg) for $k = 0.2$ overlaid with swirling strength contour for (*a*) flexible LE, (*b*) flexible TE, and (*c*) rigid foils

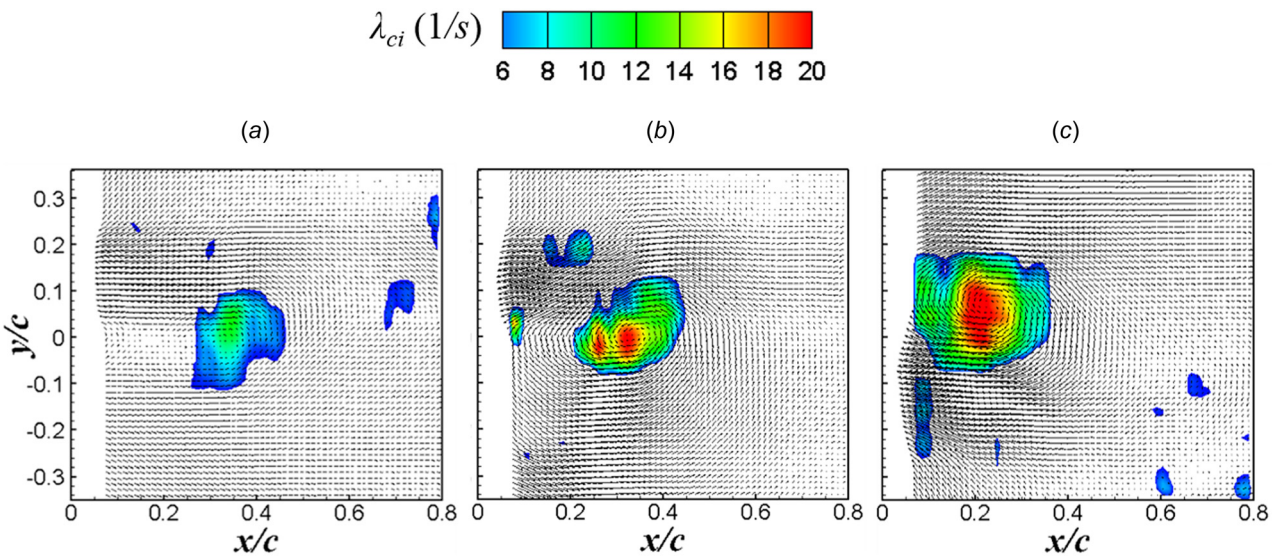

Fig. 8 Instantaneous large-scale LES filtered velocity for the flexible LE case overlaid with swirling strength based on low-pass velocity field at Φ = 0 deg showing the LEV for (*a*) $k = 0.18$, (*b*) $k = 0.19$, and (*c*) $k = 0.20$

freestream velocity was subtracted from the velocity field to visualize the flow structures more clearly. The instantaneous swirling strength field shows that the size of the LEV increases with increasing frequency, but the peak value remains relatively constant at $\lambda_{ci} \approx 16$–19 1/s. Additionally, as the reduced frequency increases, the LEV is detected at a location closer to the trailing edge. This may be because at smaller reduced frequencies the deflection amplitude of the LE is smaller, causing the LEV to shed at an earlier time during the cycle. Another reason may be that the vortex convective velocity decreases with increasing reduced frequency, and so the case with $k = 0.2$ results in the slower convecting LEV, thus locating it closer to the trailing edge as compared to the rigid and flexible TE foils.

To better understand influence of surface flexibility on the coherence and dynamics of wake vortical flow structures, the temporal and spatial scales of these events were evaluated. The spatial autocorrelations were determined for the full range of reduced frequencies using the longitudinal turbulent fluctuation velocity component, u', defined as

$$\langle \rho_{u'u'} \rangle \frac{\overline{u'(x)u'(x+\Delta x)}}{\overline{u'(x)}} \tag{2}$$

where $\langle \rho_{u'u'} \rangle$ is the averaged autocorrelation function. Due to the oscillatory motion of the foil, the fluctuating velocity is obtained by using the triple decomposition of the velocity [48]

$$u = \overline{u} + \tilde{u} + u' \tag{3}$$

where u is the instantaneous velocity field, $\overline{u}$ is the time-averaged velocity field, $\tilde{u}$ is the periodic velocity fluctuation, and u' is the turbulent velocity fluctuation. By adding the time-averaged velocity field to the periodic fluctuations of a specific phase, the phase-averaged velocity component becomes

$$\langle u \rangle = \overline{u} + \tilde{u} \tag{4}$$

By phase-locking the PIV measurements on a specific phase during the heaving cycle, the phase-averaged velocity component is determined. Therefore, the velocity fluctuations pertaining to one phase is

$$u' = u - \langle u \rangle \tag{5}$$

For each phase, the autocorrelation was calculated and the results were averaged to obtain an average autocorrelation function throughout the cycle. The results are shown in Fig. 9. Note that the spatial shift in the horizontal direction, Δx, is normalized by the total heaving amplitude A. For all k values, the autocorrelation function drops rapidly regardless of the LE or TE flexibility, indicating a lack of small to intermediate scale structure coherence. The autocorrelation function shows a periodic pattern for $k = 0.09$ and 0.12, for all three foil configurations. This is consistent with the vortex street wake configuration shown in Fig. 5. At these lower reduced frequencies, the LEV does not develop and the vortex structures are formed due to the shedding of the boundary layer at the trailing edge, resulting in an organized von Kármán vortex street. The peak-to-peak distance of the periodic pattern represents the vortex separation length scale and is approximately equal to $0.55A$. As the reduced frequency is increased to $k = 0.18$ and 0.20, a large-scale LEV is developed which results in a slower rate of decay of the autocorrelation function and the elimination of the organized vortex shedding pattern, as evidenced in the phase-averaged vorticity distribution in Fig. 5. For the flexible TE and rigid foils, the autocorrelation functions are shown to collapse together indicating that the oscillation frequency and foil flexibility at the trailing edge has little influence on the spatial coherence of the vortical structures. Similarly, the vortex separation length for the flexible LE foil at low reduced frequencies remains constant near $0.55A$. This is verified by physically estimating the separation distance between two consecutive vortices (in the same row) from instantaneous small-scale LES filtered velocity fields (e.g., Fig. 7). It can be seen that the separation distance is approximately equal to $0.14c$, which is equivalent to $0.56A$.

To determine the length scale of the largest structures in the wake, L, the value of $\Delta x/A$ at which the autocorrelation function first drops to 0 was used. This was done instead of attempting to integrate the autocorrelation to the first zero crossing due to the lack of resolution at the very small scales of $\langle \rho_{u'u'} \rangle$. Also, the scaling is based on the total amplitude of heaving, A, to provide a better comparison of its size relative to the cross-stream dimension of the wake. The results of the normalized length scale as a function of reduced frequency are shown in Fig. 10. At low values of k, the length scale for all foil configurations is $L \sim 0.2A$. For the rigid and flexible TE cases, increasing the reduced frequency slightly increases the length scale to about $0.25A$. This result is similar to the vortex diameter estimated from the instantaneous swirling

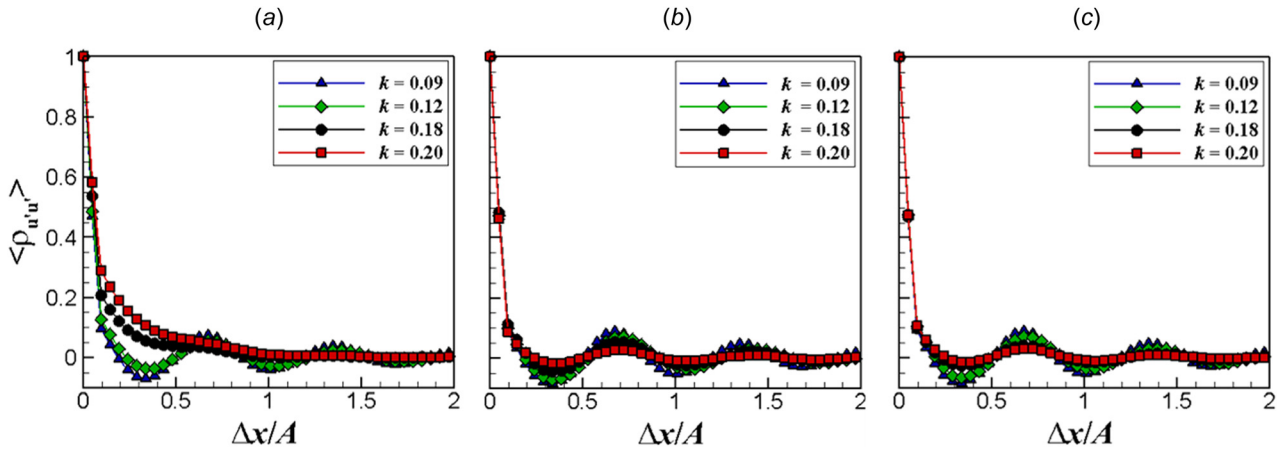

Fig. 9 Autocorrelation of the longitudinal turbulent velocity for $k = 0.09$, 0.12, 0.18, and 0.2 for (*a*) flexible LE, (*b*) flexible TE, and (*c*) rigid foils

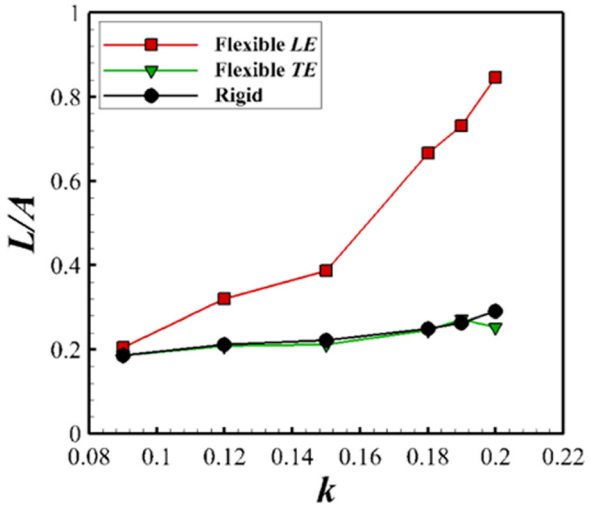

Fig. 10 Normalized length scale based on the longitudinal velocity fluctuations as a function of *k* for the flexible LE, TE, and rigid foils

strength distribution, such as that of Fig. 7. It should be noted that a cutoff of $\lambda_{ci} = 14$ 1/s for the swirling strength data was used in Fig. 7 in order to visualize the vortex structures more clearly. For the flexible LE case, it is seen that the length scale increases as k increases somewhat from 0.09 to 0.15, and then rapidly increases for $k \geq 0.18$. The second increase in length scale is associated with the development of the LEV at the higher reduced frequencies. At the highest reduced frequency case, the LEV spans almost the entire width of the wake, with $L \sim 0.85A$. This may also be confirmed by estimating the diameter of the LEV from the large-scale LES filtered velocity field, given in Fig. 8. The length scales determined from the autocorrelation and direct estimate are summarized in Table 2. Using the autocorrelation zero crossing or the swirling strength based on high- or low-pass filtering results in approximately the same vortical scale size estimates in the near wake.

Table 2 Vortical length scale estimates

	Autocorrelation function	Direct estimate (LES)
Vortex street elements	$\sim 0.2A - 0.30A$	$\sim 0.17A - 0.26A$
Leading edge vortex (LEV at $k = 0.18$–0.2)	$\sim 0.7A - 0.85A$	$\sim 0.68A - 0.90A$

The time scales associated with the wake flow vortical elements are both the swirl characteristic time scale and the convective time scale. As previously discussed, the swirling strength, λ_{ci}, is a direct measure of the inverse of the period required for a vortex to complete one revolution about its axis. Therefore, it can be thought of as a measure of the swirling frequency, or inverse of the swirling time scale. To calculate λ_{ci} for individual swirling structures, the procedure described by Patil and Liburdy [49] is used, whereby after obtaining the swirling strength field, a background threshold of 10% of the maximum value was subtracted from each instantaneous swirl field. The swirl data were then processed to determine the local maximum λ_{ci} within each swirl region. The local maximum was used to define the swirling strength of an individual vortex. Furthermore, the convective velocity associated with each vortex was determined by extracting the velocity from the low-pass filtered LES velocity field, using the coordinates of the location of the local maximum swirl. This was performed on each instantaneous field from the phase-locked PIV measurements, and then, the average of the maximum swirling strength, $\langle \lambda_{ci} \rangle$, and mean convective velocity, $\langle u_{\text{conv}} \rangle$, of all four phases was calculated. The results are shown in Fig. 11. It is seen that as the reduced frequency increases, the mean swirling strength, $\langle \lambda_{ci} \rangle$, decreases, resulting in an increase of the mean rotational time scale ($1/\langle \lambda_{ci} \rangle$) of the vortical structures. In addition, for all reduced frequencies, the flexible TE foil has a higher mean swirling strength compared to both the rigid and flexible LE foils. Similar results were obtained by Heathcote and Gursul [31]. Moreover, the flexible LE foil generates vortical elements with the lowest mean swirling strength. The inverse relationship between swirling strength and reduced frequency is believed to be associated with stronger tip vortices for the higher heaving frequencies acting on the wake vortical structures. For low aspect ratio foils, it has been observed that tip vortices tend to compress the spanwise wake vortical structures at the midspan, thus increasing their size and diminishing their strength [50]. This may be a contributor to the lower swirling frequency at higher reduced frequencies since the spanwise vortical elements would be affected more strongly as the oscillation frequency increases. Figure 11(*b*) shows the mean vortex convective velocity normalized by the freestream velocity. For $k < 0.18$, the convective velocities of all foil configurations are roughly equal (note the expanded scale). For $k \geq 0.18$, the flexible LE foil shows a sharp drop from $\langle u_{\text{conv}} \rangle / U \approx 0.92$ to $\langle u_{\text{conv}} \rangle / U \approx 0.83$. The reduction in convective velocity is believed to be a result of the formation of the LEV, since, *on average*, the small-scale eddies inside the LEV are convected downstream with the same velocity as the LEV (i.e., they move together). The trend of convective velocity of the LEV versus the reduced frequency in this study is in good agreement with the findings of Wong and Rival [51]. Overall, these are typical values

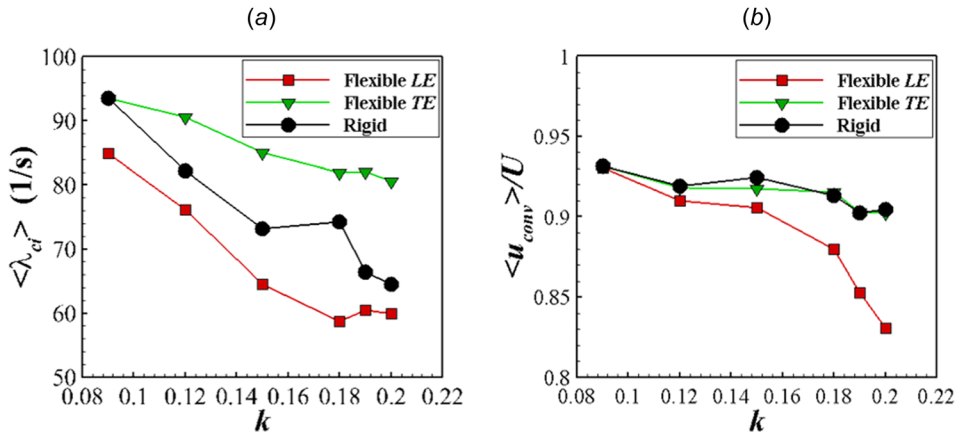

Fig. 11 The variation of (*a*) mean swirling strength and (*b*) mean convective velocity as a function of *k*

of vortex convective velocities, and similar results are reported in the literature [50,51].

The swirling time scale of the LEV for the flexible LE foil at $k = 0.18$–0.2 can be estimated from the mean swirling strength of the low-pass LES filtered velocity field. The results are shown in Fig. 12. Once the LEV develops beyond $k = 0.18$, its mean swirling strength remains constant at approximately 17 1/s. So, larger reduced frequencies result in a longer residence of LEV (smaller convective velocities) along with no noticeable reduction in swirling strength. This suggests that the foil with a flexible LE at large reduced frequencies has the potential to increase the cycle-averaged lift forces as the LEV resides near the surface longer, without loss of strength. Interestingly, the small-scale structures inside the LEV for $k = 0.18$–0.2 for the flexible LE case also remain approximately constant with increasing reduced frequency. The ratio of the swirling strength of the small-scale structures to that of the LEV is approximately 3.5, indicating that the small-scale structures in the LEV, on average, rotate approximately 3.5 times faster than that of the LEV. A future study is required to examine the interaction between the large-scale structures and smaller scale eddies in further detail.

Wake Energy Deficit. The periodic velocity component ($\tilde{u}$) from the velocity triple decomposition given in Eq. (3) is related to flow structures whose formation and evolution are dependent on the foil motion (i.e., phase related with the oscillation motion).

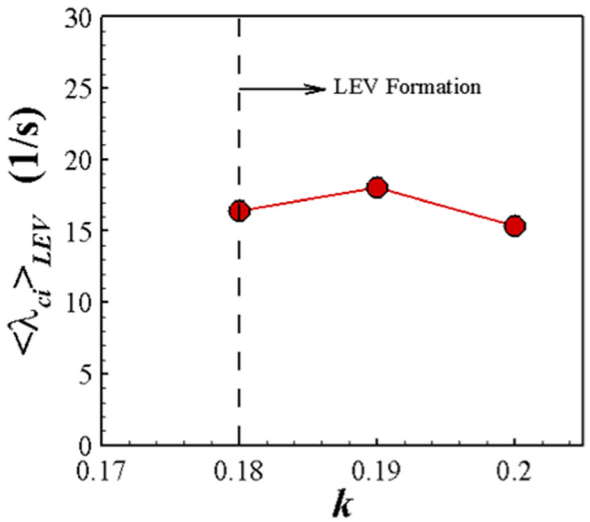

Fig. 12 Mean swirling strength of the LEV as a function of *k*

These flow structures extract momentum/energy from the mean flow, whereas the turbulent structures, represented by u', extract energy from the mean flow as well as the periodic structures [52,53]. However, only relatively large structures tend to be efficient at extracting energy, whereas the smaller scale eddies tend to be more efficient at the dispersion processes [54–56]. It is shown in Fig. 3 that increasing the reduced frequency has a negligible influence on the amount of momentum/energy deficit in the mean flow for the flexible TE and rigid foils. From these profiles, both of these foils exhibit similar values of mean energy deficit. The flexible LE foil also results in similar characteristics but only for $k < 0.18$. The question is whether or not, at the higher reduced frequencies, a large scale LEV is generated only for the flexible LE condition. The periodic flow structures that are formed for these cases are relatively small (comparable to the small-scale structures visualized by the LES technique in Fig. 7). Therefore, the amount of energy extracted by the vortical structures from the mean flow does not change with increasing frequency, and the vortices only act to transport the momentum in the wake. On the contrary, the flexible LE foil at high reduced frequencies generates a large periodic structure (LEV) that captures energy from the mean flow, hence resulting in a large energy deficit, as can be seen in Fig. 3. The average kinetic energy lost in the wake at any x/c location can be calculated as

$$\mathrm{KE}_{\mathrm{deficit}} = \frac{1}{Y}\int_{-\infty}^{\infty}\left(U^2 - \overline{u}(y)^2\right)dy \tag{6}$$

where U is the freestream velocity, $u'(y)$ is the time-averaged vertical velocity distribution, and Y is the width of the wake. The velocity profiles in Fig. 3 were used to evaluate the integral in Eq. (6). Furthermore, a scale of the energy content per unit mass of the LEV was determined based on the LEV length scale and rotational time scale data from Figs. 10 and 12, respectively. The resulting scaling is $(\lambda_{ci}^2 L^2)_{\mathrm{LEV}}$. The variations of $(\lambda_{ci}^2 L^2)_{\mathrm{LEV}}$ and $\mathrm{KE}_{\mathrm{deficit}}$ at $x/c = 0.2$ with reduced frequency are shown in Fig. 13. It is seen that $(\lambda_{ci}^2 L^2)_{\mathrm{LEV}}$ and $\mathrm{KE}_{\mathrm{deficit}}$ follow similar trends of increasing value with increasing k. Based on this, as the reduced frequency increases, the LEV captures more energy from the mean flow (represented by $(\lambda_{ci}^2 L^2)_{\mathrm{LEV}}$), which shows up as an increasing energy deficit in the near wake (represented by $\mathrm{KE}_{\mathrm{deficit}}$). As can be seen from Figs. 10 and 12, the increase of energy within the LEV is due to increased size, L, with the swirling strength remaining approximately constant. The fact that these two quantities match reasonably well indicates that the LEV is the dominant mechanism for wake energy loss. The increasing difference between the scaled LEV energy and $\mathrm{KE}_{\mathrm{deficit}}$ is most likely added energy loss by entrainment at higher heaving frequencies.

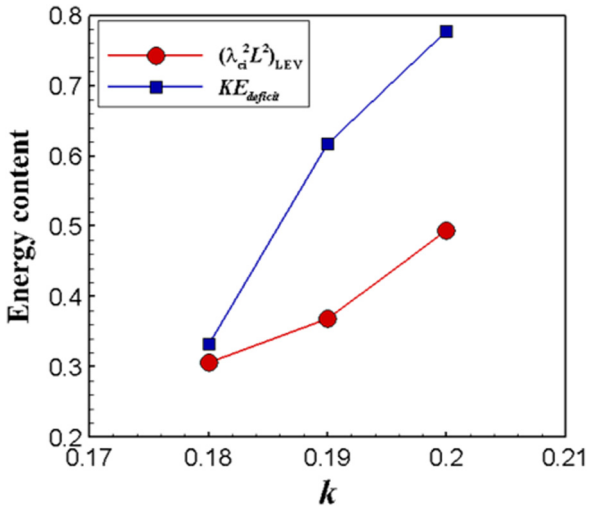

Fig. 13 Variation of energy content of the LEV structure and kinetic energy loss in the wake at $x/c = 0.2$ as a function of k

Future work will be conducted to evaluate the interaction between the mean, periodic, and turbulent flow structures in more detail.

Conclusions

Detailed measurements using time-resolved and phase-resolved PIV were obtained in the near-wake region of a heaving foil with flexibility at the leading and trailing edges as well as for a fully rigid foil over a reduced frequency range from 0.09 to 0.2. The data were analyzed to describe the influence of flexibility on the wake dynamics. The results obtained in this study are useful in flapping wing applications, especially when operating in the energy harvesting flow regime. It is shown that surface flexibility at the leading edge has potential to significantly enhance the lift force during a heaving cycle.

The time-averaged velocity and vorticity were shown to exhibit similar characteristics for the flexible trailing edge and rigid foils. For the range of reduced frequencies evaluated, the mean momentum deficit for both foils is found to remain constant, and the vortex shedding dynamics is shown to behave in a manner similar to blunt bodies. On the contrary, the flexible leading edge foil causes a significant mean momentum reduction for $k \geq 0.18$. At these high reduced frequencies, the heaving inertia results in a large deflection amplitude of the leading edge. As a consequence, the adverse pressure gradient increases such that the boundary layer separation at the leading edge creates a large-scale LEV, which is shown to shed at the top and bottom of the heaving positions. Furthermore, swirling strength analysis, LES decomposition, and autocorrelation of velocity fluctuations were used to accurately quantify the vortex statistics in the wake region. The results demonstrate that the trailing edge flexibility results in an enhanced swirling strength of the small-scale vortical structures, which act to disperse the mean momentum, creating a wider wake region when compared to the rigid foil. On the other hand, the flexible leading edge results in a decrease in the small-scale vortex strength, and a significant increase in the length scales with increasing reduced frequencies. For $k \geq 0.18$, it is shown that the large-scale LEVs have a size comparable to that of the heaving amplitude. The swirling strength technique was applied on the low-pass LES filtered velocity fields to determine the strength of the LEV. It is found that its strength remains relatively constant with increasing reduced frequency. Finally, it is shown that the large-scale LEV is the main contributor in extracting energy from the mean flow, which results in a significant reduction in the kinetic energy of the mean flow. A vortex energy scaling of $\lambda_{ci}^2 L^2$, which is used to estimate the LEV energy content, is shown to correlate well with the kinetic energy loss in the wake. Future work will be conducted to examine the interaction between the mean flow and periodic flow structures (LEV) as well as the turbulent eddies.

Acknowledgment

The authors would like to thank Ali Mousavian and Cameron Planck for their assistance in the experimental setup.

Nomenclature

A = heaving amplitude
c = foil chord length
f = oscillation frequency
$k = fc/U$ = reduced frequency
L = vortex length scale
Re = Reynolds number
t = time
T = oscillation period
u = instantaneous velocity
U = freestream velocity
$\overline{u}$ = time-averaged velocity
u' = turbulent velocity
$\tilde{u}$ = periodic velocity
$\langle u \rangle$ = phase-averaged velocity
x = longitudinal direction
y = transverse direction

Greek Symbols

θ = deflection angle
λ_{ci} = swirling strength
ρ = autocorrelation function
Φ = heaving phase
ω = vorticity

References

[1] Drucker, E. G., and Lauder, G. V., 2000. "A Hydrodynamic Analysis of Fish Swimming Speed: Wake Structure and Locomotor Force in Slow and Fast Labriform Swimmers," J. Exp. Biol., **203**(16), pp. 2379–2393.
[2] Lauder, G. V., Madden, P. G. A., Mittal, R., Dong, H., and Bozkurttas, M., 2006, "Locomotion With Flexible Propulsors: I. Experimental Analysis of Pectoral Fin Swimming in Sunfish," Bioinspir. Biomim., **1**(4), pp. S25–S34.
[3] Triantafyllou, M. S., Triantafyllou, G. S., and Yue, D. K. P., 2000, "Hydrodynamics of Fishlike Swimming," Annu. Rev. Fluid Mech., **32**(1), pp. 33–53.
[4] Ramamurti, R., Sandberg, W. C., Löhner, R., Walker, J. A., and Westneat, M. W., 2002, "Fluid Dynamics of Flapping Aquatic Flight in the Bird Wrasse: Three-Dimensional Unsteady Computations With Fin Deformation," J. Exp. Biol., **205**(19), pp. 2997–3008.
[5] Drucker, E. G., and Lauder, G. V., "Experimental Hydrodynamics of Fish Locomotion: Functional Insights From Wake Visualization," Integr. Comp. Biol., **42**(2), pp. 243–257.
[6] Xu, J., and Sun, H., 2015, "Fluid Dynamics Analysis of Passive Oscillating Hydrofoils for Tidal Current Energy Extracting," 2015 IEEE International Conference on Mechatronics and Automation (ICMA), Beijing, China, Aug. 2–5, pp. 2017–2022.
[7] Jones, K. D., Bradshaw, C. J., Papadopoulos, J., and Platzer, M. F., 2005, "Bio-Inspired Design of Flapping-Wing Micro Air Vehicles," Aeronaut. J., **109**(1098), pp. 385–394.
[8] Jones, K. D., Davids, S. T., and Platzer, M. F., 1999, "Oscillating-Wing Power Generation," 3rd *ASME/JSME* Joint Fluids Engineering Conference, San Francisco, CA, July 18–23, FEDSM99-7050.
[9] Apte, S. V., and Base, W.-P. A., 2011, "Low Reynolds Number Flow Dynamics and Control of a Pitching Airfoil With Elastically Mounted Flap Actuator," ASEE Summer Faculty Fellowship Program, June 19–Aug. 26, Wright-Patterson Air Force Base, OH.
[10] Anderson, J. M., Streitlien, K., Barrett, D. S., and Triantafyllou, M. S., 1988, "Oscillating Foils of High Propulsive Efficiency," J. Fluid Mech., **360**, pp. 41–72.
[11] Drost, K. J., Johnson, H., Apte, S. V., and Liburdy, J. A., 2011, "Low Reynolds Number Flow Dynamics of a Thin Airfoil With an Actuated Leading Edge," AIAA Paper No. 2011-3904.
[12] Visbal, M. R., Gordnier, R. E., and Galbraith, M. C., 2009, "High-Fidelity Simulations of Moving and Flexible Airfoils at Low Reynolds Numbers," Exp. Fluids, **46**(5), pp. 903–922.

[13] Von Ellenrieder, K. D., Parker, K., and Soria, J., 2003, "Flow Structures Behind a Heaving and Pitching Finite-Span Wing," J. Fluid Mech., **490**, pp. 129–138.
[14] Parker, K., Von Ellenrieder, K. D., and Soria, J., 2007, "Morphology of the Forced Oscillatory Flow Past a Finite-Span Wing at Low Reynolds Number," J. Fluid Mech., **571**, pp. 327–357.
[15] Warrick, D. R., Tobalske, B. W., and Powers, D. R., 2005, "Aerodynamics of the Hovering Hummingbird," Nature, **435**(7045), pp. 1094–1097.
[16] Zhu, Q., 2012, "Energy Harvesting by a Purely Passive Flapping Foil From Shear Flows," J. Fluids Struct., **34**, pp. 157–169.
[17] Huxham, G. H., Cochard, S., and Patterson, J., 2012, "Experimental Parametric Investigation of an Oscillating Hydrofoil Tidal Stream Energy Converter," 18th Australasian Fluid Mechanics Conference (AFMC), Launceston, Australia, Dec. 3–7.
[18] Ashraf, K., Khir, M. H. M., and Dennis, J. O., 2011, "Energy Harvesting in a Low Frequency Environment," National Postgraduate Conference (NPC), Kuala Lumpur, Malaysia, Sept. 19–20.
[19] Peng, Z., and Zhu, Q., 2009, "Energy Harvesting Through Flow-Induced Oscillations of a Foil," Phys. Fluids, **21**(12), p. 123602.
[20] Jones, K. D., and Platzer, M. F., 1997, "Numerical Computation of Flapping-Wing Propulsion and Power Extraction," AIAA Paper No. 97-0826.
[21] McKinney, W., and DeLaurier, J., "Wingmill: An Oscillating-Wing Windmill," J. Energy, **5**(2), pp. 109–115.
[22] Kinsey, T., and Dumas, G., 2012 "Computational Fluid Dynamics Analysis of a Hydrokinetic Turbine Based on Oscillating Hydrofoils," ASME J. Fluids Eng., **134**(2), p. 021104.
[23] Heathcote, S., Martin, D., and Gursul, I., 2004, "Flexible Flapping Airfoil Propulsion at Zero Freestream Velocity," AIAA J., **42**(11), pp. 2196–2204.
[24] Youcef-Toumi, K., 2005, "Performance of Machines With Flexible Bodies Designed for Biomimetic Locomotion in Liquid Environments," 2005 IEEE International Conference on Robotics and Automation (ICRA 2005), Apr. 18–22, pp. 3324–3329.
[25] Miao, J.-M., and Ho, M.-H., 2006, "Effect of Flexure on Aerodynamic Propulsive Efficiency of Flapping Flexible Airfoil," J. Fluids Struct., **22**(3), pp. 401–419.
[26] Shyy, W., and Liu, H., 2007, "Flapping Wings and Aerodynamic Lift: The Role of Leading-Edge Vortices," AIAA J., **45**(12), pp. 2817–2819.
[27] Heathcote, S., Wang, Z., and Gursul, I., 2008, "Effect of Spanwise Flexibility on Flapping Wing Propulsion," J. Fluids Struct., **24**(2), pp. 183–199.
[28] Zhao, L., Huang, Q., Deng, X., and Sane, S. P., 2010, "Aerodynamic Effects of Flexibility in Flapping Wings," J. R. Soc. Interface, **7**(44), pp. 485–497.
[29] Gopalakrishnan, P., and Tafti, D. K., "Effect of Wing Flexibility on Lift and Thrust Production in Flapping Flight," AIAA J., **48**(5), pp. 865–877.
[30] Kang, C.-K., Aono, H., Cesnik, C. E. S., and Shyy, W., 2011, "Effects of Flexibility on the Aerodynamic Performance of Flapping Wings," J. Fluid Mech., **689**, pp. 32–74.
[31] Heathcote, S., and Gursul, I., 2007, "Flexible Flapping Airfoil Propulsion at Low Reynolds Numbers," AIAA J., **45**(5), pp. 1066–1079.
[32] Wu, J., Wu, J., Tian, F.-B., Zhao, N., and Li, Y.-D., 2015, "How a Flexible Tail Improves the Power Extraction Efficiency of a Semi-Activated Flapping Foil System: A Numerical Study," J. Fluids Struct., **54**, pp. 886–899.
[33] Siala, F., and Liburdy, J. A., 2015, "Energy Harvesting of a Heaving and Forward Pitching Wing With a Passively Actuated Trailing Edge," J. Fluids Struct., **57**, pp. 1–14.
[34] Liu, W., Xiao, Q., and Cheng, F., 2013, "A Bio-Inspired Study on Tidal Energy Extraction With Flexible Flapping Wings," Bioinspir. Biomim., **8**(3), p. 36011.
[35] Bandyopadhyay, P. R., 2016, "Swimming and Flying in Nature—The Route Toward Applications: The Freeman Scholar Lecture," ASME J. Fluids Eng., **131**(3), p. 031801.
[36] Zhao, L., Deng, X., and Sane, S. P., 2011, "Modulation of Leading Edge Vorticity and Aerodynamic Forces in Flexible Flapping Wings," Bioinspir. Biomim., **6**(3), p. 36007.
[37] Shoele, K., and Zhu, Q., 2012, "Leading Edge Strengthening and the Propulsion Performance of Flexible Ray Fins," J. Fluid Mech., **693**, pp. 402–432.
[38] Gursul, I., Wang, Z., and Vardaki, E., 2007, "Review of Flow Control Mechanisms of Leading-Edge Vortices," Prog. Aerosp. Sci., **43**(7), pp. 246–270.
[39] Lai, J. C. S., and Platzer, M. F., 1999, "Jet Characteristics of a Plunging Airfoil," AIAA J., **37**(12), pp. 1529–1537.
[40] Lua, K. B., Lim, T. T., Yeo, K. S., and Oo, G. Y., 2007, "Wake-Structure Formation of a Heaving Two-Dimensional Elliptic Airfoil," AIAA J., **45**(7), pp. 1571–1583.
[41] von Ellenrieder, K. D., and Pothos, S., 2008, "PIV Measurements of the Asymmetric Wake of a Two Dimensional Heaving Hydrofoil," Exp. Fluids, **44**(5), pp. 733–745.
[42] Lewin, G. C., and Haj-Hariri, H., 2003, "Modelling Thrust Generation of a Two-Dimensional Heaving Airfoil in a Viscous Flow," J. Fluid Mech., **492**, pp. 339–362.
[43] Koochesfahani, M. M., 1989, "Vortical Patterns in the Wake of an Oscillating Airfoil," AIAA J., **27**(9), pp. 1200–1205.
[44] Young, J., and Lai, J. C. S., 2004, "Oscillation Frequency and Amplitude Effects on the Wake of a Plunging Airfoil," AIAA J., **42**(10), pp. 2042–2052.
[45] Westerweel, J., 2008, "On Velocity Gradients in PIV Interrogation," Exp. Fluids, **44**(5), pp. 831–842.
[46] Zhou, J., Adrian, R. J., Balachandar, S., and Kendall, T. M., 1999, "Mechanisms for Generating Coherent Packets of Hairpin Vortices in Channel Flow," J. Fluid Mech., **387**, pp. 353–396.
[47] Adrian, R. J., Christensen, K. T., and Liu, Z.-C., 2000, "Analysis and Interpretation of Instantaneous Turbulent Velocity Fields," Exp. Fluids, **29**(3), pp. 275–290.
[48] Hussain, A. K. M. F., and Reynolds, W. C., 1970, "The Mechanics of an Organized Wave in Turbulent Shear Flow," J. Fluid Mech., **41**(02), pp. 241–258.
[49] Patil, V. A., and Liburdy, J. A., 2013, "Flow Structures and Their Contribution to Turbulent Dispersion in a Randomly Packed Porous Bed Based on Particle Image Velocimetry Measurements," Phys. Fluids, **25**(11), p. 113303.
[50] Dong, H., Mittal, R., and Najjar, F. M., 2006, "Wake Topology and Hydrodynamic Performance of Low-Aspect-Ratio Flapping Foils," J. Fluid Mech., **566**, pp. 309–343.
[51] Wong, J. G., and Rival, D. E., 2015, "Determining the Relative Stability of Leading-Edge Vortices on Nominally Two-Dimensional Flapping Profiles," J. Fluid Mech., **766**, pp. 611–625.
[52] Panda, J., and Zaman, K., 1994, "Experimental Investigation of the Flow Field of an Oscillating Airfoil and Estimation of Lift From Wake Surveys," J. Fluid Mech., **265**, pp. 65–95.
[53] Rival, D., Prangemeier, T., and Tropea, C., 2009, "The Influence of Airfoil Kinematics on the Formation of Leading-Edge Vortices in Bio-Inspired Flight," Exp. Fluids, **46**(5), pp. 823–833.
[54] Hussain, A. K. M. F., 1983, "Coherent Structures—Reality and Myth," Phys. Fluids, **26**(10), pp. 2816–2850.
[55] Sarkar, A., and Schlüter, J., 2013, "Numerical Investigation of the Turbulent Energy Budget in the Wake of Freely Oscillating Elastically Mounted Cylinder at Low Reduced Velocities," J. Fluids Struct., **43**, pp. 441–462.
[56] Tennekes, H., and Lumley, J. L., 1972, *A First Course in Turbulence*, MIT Press, Cambridge, MA.